

Accepted Manuscript

Geological Society, London, Special Publications

Morphology and spatio-temporal distribution of lacustrine mass-transport deposits in Wörthersee, Eastern Alps, Austria

Christoph Daxer, Maddalena Sammartini, Ariana Molenaar, Thomas Piechl, Michael Strasser & Jasper Moernaut

DOI: <https://doi.org/10.1144/SP500-2019-179>

Received 30 September 2019

Revised 14 November 2019

Accepted 20 November 2019

© 2019 The Author(s). Published by The Geological Society of London. All rights reserved. For permissions: <http://www.geolsoc.org.uk/permissions>. Publishing disclaimer: www.geolsoc.org.uk/pub_ethics

To cite this article, please follow the guidance at <https://www.geolsoc.org.uk/onlinefirst#how-to-cite>

Manuscript version: Accepted Manuscript

This is a PDF of an unedited manuscript that has been accepted for publication. The manuscript will undergo copyediting, typesetting and correction before it is published in its final form. Please note that during the production process errors may be discovered which could affect the content, and all legal disclaimers that apply to the book series pertain.

Although reasonable efforts have been made to obtain all necessary permissions from third parties to include their copyrighted content within this article, their full citation and copyright line may not be present in this Accepted Manuscript version. Before using any content from this article, please refer to the Version of Record once published for full citation and copyright details, as permissions may be required.

Morphology and spatio-temporal distribution of lacustrine mass-transport deposits in Wörthersee, Eastern Alps, Austria

Christoph Daxer^{1*}, and Maddalena Sammartini¹, and Ariana Molenaar¹, and Thomas Piechl², and Michael Strasser¹ and Jasper Moernaut¹

¹*Institute of Geology, University of Innsbruck, Austria*

²*Amt der Kärntner Landesregierung, Klagenfurt, Austria*

**Correspondence (e-mail: Christoph.Daxer@uibk.ac.at)*

Lacustrine MTD morphology in Wörthersee

Abstract: In lakes, landslides can be studied in high resolution due to their accessibility and limited size. Here, we investigated mass-transport deposits in glacial lacustrine Wörthersee (Eastern European Alps) by integration of seismic, sediment core and multibeam bathymetric data. Two outstanding landslide events were revealed: the first occurred in the Late Glacial, leading to multiple deposits of up to 15 m thickness; they consist of sandy turbidites and mudclast conglomerates, which are overlain by a 2.5 m thick megaturbidite. The extensive, likely earthquake-triggered failure linked to this event was preconditioned by rapid sedimentation of fine-grained glaciolacustrine sediments and associated build-up of excess pore pressure. The second event was presumably triggered by a major earthquake ($M_w \sim 7$) in AD1348 and comprises a mass-transport complex and several landslides, which led to a ~30 cm thick turbidite. In total, 62 landslides are imaged in the multibeam map, of which 6 are most likely human-induced. Some of these show horseshoe-type compressional ridges and frontal breaching, whereas others exhibit an extensive zone of rafted blocks. We attribute these morphological differences to four main factors: 1) slope gradient and changes therein; 2) preconditioning of the impacted zone; 3) volume of remobilized sediment and (4) and type of impactor.

Other than their often devastating consequences, including tsunamis (Bondevik *et al.* 2005; Tappin *et al.* 2008; Urgeles *et al.* 2019) or loss of infrastructure (Assier-Rzadkiewicz *et al.* 2000; Pope *et al.* 2017), the processes involved in initiation, propagation and emplacement of submarine landslides cannot be readily monitored (Masson *et al.* 2006). Therefore, we either rely on physical or numerical models (Rzadkiewicz *et al.* 1996; Enet *et al.* 2003; Bondevik *et al.* 2005; Sue *et al.* 2011) or detailed characterization of the landslide morphology in source-, translation- and deposition-area (Hühnerbach & Masson 2004; Twichell *et al.* 2009; Urgeles & Camerlenghi 2013) in order to understand the fundamental mechanisms underlying submarine mass movements. Comparison of these processes in the oceanic (Owen *et al.* 2007; Krastel *et al.* 2014 and references therein) and lacustrine realm (Girardclos *et al.* 2007; Moernaut & De Batist 2011; Wiemer *et al.* 2015) indicate broad similarities, allowing us to use the smaller and more easily accessible lacustrine landslides as a natural laboratory for the ocean (Sammartini *et al.*, in press; Strasser *et al.* 2007).

Slope failures are often ultimately triggered by a single event, e.g. earthquakes (Piper *et al.* 1999), cyclones (Pope *et al.* 2017), or sudden gravitational loading (Assier-Rzadkiewicz *et al.* 2000). Nevertheless, sediment accumulation rates, deposition of lithologically varying sediments (L'Heureux *et al.* 2012) as well as the development of excess pore pressure (Talling *et al.* 2014) are important preconditioning factors, acting on longer timescales (Urgeles & Camerlenghi 2013). In order to statistically assess the influence of such time-dependent factors on slope stability and understand the hazard potential of slope failures, knowledge about the spatio-temporal variability of landslides in both marine and lacustrine environments is of paramount importance (Masson *et al.* 2006).

Glacigenic lakes in temperate climates offer the possibility to investigate the influence of changing sedimentary properties (from glacio-lacustrine to hemipelagic sediments) and – due to the small dimensions of most lakes – the critical stratigraphic levels can often be sampled via standard piston coring techniques. Moreover, accurate dating of landslide events reaching back into Late Glacial time is possible due to the general abundance of organic macro-remains for ^{14}C dating and the possible presence of annual laminations (varves). Limited water depths allow for very-high resolution morphologic and seismic-stratigraphic mapping. In the present study, we describe the morphology and seismic-stratigraphic character of landslide deposits in an Austrian glacigenic lake, from very recent, human-induced events, to extensive basin collapses in the Late Glacial. We focus on addressing research questions such as: (1) Why do some mass transport deposits (MTDs) have numerous rafted blocks whereas others seem to form more coherent masses? (2) Which factors control the potential of landslides to deform and erode basin-plain sediments? (3) To what extent are the dimensions and morphology of landslide deposits influenced by the geotechnical properties of failed slope sequences?

Geological and geomorphological setting

Wörthersee (*See* = German for lake) is located in the Austrian state of Carinthia (Eastern European Alps), near the border to Italy and Slovenia (Fig. 1). The lake covers 19.4 km² and is embedded in a glacially overprinted landscape consisting of metamorphic crystalline units (phyllites & mica-schists; Homann 1962). The three main lake basins as well as their sub-basins (Kapuziner-, Reifnitz- and Klagenfurt basin) are separated by bedrock and/or moraine ridges and follow the trend imposed by a series of WSW-ENE striking (transform) faults and their associated auxiliary faults (Kahler 1962; Anderle 1977; Pistotnik *et al.* 1980).

Wörthersee reaches its maximum depth (84 m) in the western basin, which mainly exhibits steep ($> 15^\circ$) slopes. In the middle basin (max. depth 40 m) and the eastern basin (70 m), shallow (20 m) bays and nearshore terraces are common features. Most of the lakes' inflows are small rivulets entering the western lake basin, altogether draining a catchment area of 162 km². The main inflow enters the lake near Reifnitz at an average discharge of 0.63 m³/s. The only outlet, the artificially regulated Glanfurt, leaves the lake in the very east near Klagenfurt. According to the Carinthian Institute for Lake Research (KIS), the lake level dropped severely around AD1770, when construction activity at the Glanfurt was completed (KIS 2019). Human influence is also clearly visible along the shoreline, of which only 23% remain in a natural to near-natural state. The remaining 77% either have been reinforced (47%) or altered by human activity (30%; Schulz *et al.* 2008). On 11 December 2013, a landslide happened at a construction site located near Bad Saag at the northern shore of the western lake basin (Fig. 1). Dug-out material as well as 3 containers were placed close to the shoreline, which then collapsed. The resulting landslide transported the containers and “several thousands of m³” (APA/derStandard 2013) of onshore material down into the lake basin, fortunately causing no fatalities.

The study area is one of Austria's seismically most active regions and has been affected by several damaging earthquakes ($M_w > 6$) in AD1348, AD1511, AD1690, and AD1976, with the AD1348 event being the strongest historical earthquake ($M_w \sim 7$) documented in the entire Alps (Stucchi *et al.* 2013). Due to its location at the south-eastern border of the Alps, deglaciation in the area surrounding Wörthersee occurred earlier than in other peri-alpine lakes (Seguinot *et al.* 2018). This is supported by radiocarbon ages from sediments in the nearby Jeserzersee (~ 2 km north of Velden; see Fig. 1), where two (bulk-)samples taken at the base of a 7.26 m long sediment core yielded ages of 17140 – 17825 cal BP and 17581 – 19366 cal BP, respectively (Schultze 1984; Schmidt *et al.* 2012).

Material and Methods

Multibeam bathymetry

Bathymetric data was acquired in 2017 using a high-resolution SeaBat T50-P multibeam echosounder combined with an AsteRx-U MARINE GNSS Heading System. Data processing was conducted with Qinsy software. The resulting bathymetric maps used in this study have a cell size of 2 m. To enhance the topography, the maps showing the detailed landslide morphologies are presented as a combination of topographic openness (Yokoyama *et al.* 2002), analytical hillshade and colour slices from the digital elevation model generated in SAGA GIS (Conrad *et al.* 2015) and combined in Adobe Illustrator software. Description and interpretation of landslide morphometric parameters was carried out in a standard GIS framework (ArcGIS 10.5.1) following Clare *et al.* 2018.

Seismic reflection data

High-resolution seismic data was acquired during three separate surveys in 2017 and 2019 using two different systems: a 3.5 kHz Geopulse pinger source (theoretical vertical resolution: ~ 10 cm; 203 km of survey lines) and an Innomar SES-2000 light sub-bottom

profiler (100 kHz primary frequency, 8 kHz secondary low frequency; theoretical vertical resolution: ~5 cm; 121 km of survey lines; Fig. 1(b)). Positioning was carried out with stand-alone GPS. The data was processed in the IHS Markit Kingdom (v. 2018) Seismic and Geological Interpretation software applying a bandpass filter for the 3.5 kHz data (lower cut 2 kHz, upper cut 6 kHz). Sedimentary deposits related to landsliding were distinguished from regular background sedimentation – exhibiting continuous reflections – by their irregular to chaotic seismic facies and intercalated geometry, which in turn differs from the mappable transparent seismic intervals and ponding geometry attributed to megaturbidites (*sensu* Schnellmann *et al.* 2002). Such deposits are herein interchangeably also referred to as mass transport deposits, MTDs, if they constitute singular, unidirectional events. For synchronous, overlapping and multi-directional event deposits, where individual landslides cannot be distinguished in the seismic data (but might be discernible in the multibeam data), the term mass transport complex, MTC, is used. Event horizons are defined as the seismic-stratigraphic horizons related to the pinch-out points of MTDs and are potentially overlain by the associated megaturbidites. These horizons were mapped over the whole lake to determine synchronicity of individual landslides (Strasser *et al.* 2013). If steep slope angles and non-sedimentation prohibited mapping of seismic event horizons over lake basin boundaries, correlation polygons were used to determine correlative seismic stratigraphic horizons. For the time-to-depth-conversions, a constant velocity of 1500 m/s for both water and sediment was assumed. Errors arising from changes in velocity are negligible (~5 cm/ms) and therefore irrelevant for the purpose of this study. Volumetric analyses were carried out in Surfer (Golden Software).

Coring campaigns and sediment core analyses

From 2017 to 2019, short (~1.5 m) sediment cores were retrieved using a percussion gravity corer. In September 2018, an ~11 m long gravity piston core (Kullenberg type; Kelts *et al.* 1986) was retrieved in the deepest part of the western basin. X-ray computed tomography (CT) scans were carried out on whole round sediment cores at the Medical University of Innsbruck, using a Siemens SOMATOM Definition AS. For data visualization, the software VGSTUDIO (v. 3.3) as well as FIJI (Schindelin *et al.* 2012) were used. γ -density and magnetic susceptibility (MS) were measured at 0.5-cm and 0.2-cm vertical resolution, respectively, using a GEOTEK Multi-Sensor Core Logger (MSCL) and a Bartington MS2E point sensor at the Austrian Core Facility for scientific core logging and scanning (Institute of Geology, Innsbruck). The grain size of untreated samples was determined with a Malvern Mastersizer 3000 laser diffractometer, applying 1 minute of ultrasonication at 40% strength before measurement. Smear slide analyses were carried out following the protocol defined by Schnurrenberger *et al.* (2003).

Chronology

AMS radiocarbon dating was conducted on terrestrial plant macro-remains at the Ion beam Physics Laboratory of ETH Zürich (Table 1). Radionuclide activity measurements (^{210}Pb and ^{137}Cs) were carried out at EAWAG (Dübendorf, Switzerland) using *CANBERRA* and *Princeton Gamma-Tech* germanium well detectors.

Results

Seismic landslide stratigraphy

The sedimentary infill of Wörthersee can be generally divided into two main seismostratigraphic units separated by a high amplitude reflection package, which is present in all lake basins at about 5.5 ms (in the middle basin) to 8.5 ms (in the western basin) sediment depth (Fig. 2, 3). The upper seismic unit 1 (SU-1) consists of a draping sedimentary succession, showing parallel, low- to intermediate-amplitude reflections. The reflections are generally continuous but partly interrupted by higher amplitudes where MTDs are present. The distinctive reflection patterns in SU-1 are similar in all lake basins and allow for a detailed seismic stratigraphic correlation (Fig. 3(b)). The underlying seismic unit 2 (SU-2) constitutes an up to 43 ms (~32 m) thick sequence. The reflection pattern, which is frequently disturbed by vertical acoustic wipe-outs, commonly onlaps onto the acoustic basement, therefore exhibiting a ponding geometry (Fig. 2, 3(a)). Due to varying seismic facies, SU-2 is further distinguished into two time-equivalent seismic subunits: seismic unit 2a (SU-2a), present only in the western basin, shows low- to intermediate-amplitude reflections and intercalated, laterally fluctuating and partly truncated high-amplitude packages; seismic unit 2b (SU-2b), constituting the majority of sedimentary infill in the middle and eastern basins, is characterized by closely spaced intermediate- to high-amplitude reflections and little lateral variation.

Of several seismic-stratigraphic MTD event horizons, which can be identified especially in the western basin, three horizons are particularly prominent and are the subject of the present study: event horizon A (EH-A) constitutes the stratigraphically highest event horizon, event horizons B (EH-B) and C (EH-C) stand out due to their many time-correlative large-volume MTDs.

In terms of MTD-volume, EH-A constitutes a minor stratigraphic event horizon (Fig. 2(a); volume = $\sim 0.08 \times 10^6 \text{ m}^3$) consisting of six individual landslides, of which four are in the western basin (see Fig. 4 for locations). These MTDs are overlain by a thin ($< 1 \text{ ms}$) sedimentary drape, thus representing rather recent MTDs.

EH-B is overlain by approximately 2.6 ms of sediment in the basins. It comprises several landslides, including a mass transport complex (MTC) in the very western area of the lake near the village of Velden ('Velden MTC'; Fig 2(a)). Compressional ridges are present in the seismic data as sub-vertical high-amplitude reflections, indicating amalgamation of individual landslides. These ridges as well as the generally irregular surface of the MTC account for a hummocky lake floor. Due to limited acoustic penetration in the central part of the Velden MTC, the absolute maximum thickness remains uncertain. In well-mappable areas, however, thickness reaches up to 15 ms (Fig. 4). Apart from the Velden MTC, seven smaller MTDs are also attributed to EH-B in the western basin, five in the middle and eight in the eastern basin, respectively. These MTDs show well-developed lateral or frontal pinch-out geometries and a related, distally fading high-amplitude reflection, that extends over the basin plain (Fig. 2(c)).

Overall, the MTDs amount to a volume of $5.6 \times 10^6 \text{ m}^3$, covering an area of $1.7 \times 10^6 \text{ m}^2$. In the western basin and in small areas between compressional ridges of the Velden MTC, a megaturbidite with a maximum thickness of 1.5 ms is present. It covers an area of $\sim 0.6 \times 10^6 \text{ m}^2$ and amounts to a volume of $\sim 0.44 \times 10^6 \text{ m}^3$ (Fig. 4).

EH-C occurs within the uppermost part of seismic unit 2 and is overlain by about 10 ms (7.5 m) of sediment in the basins. The respective MTDs cover almost entirely all lake basins, as well as the nearshore terraces in both the middle and eastern basin. In the western basin, the deposits reach a maximum thickness of 20 ms. Near the village of Velden, the overlying Velden MTC of EH-B, as well as the thick deposits of EH-C itself, strongly attenuate the seismic signal (Fig. 2(a)), making mapping of the base of EH-C difficult to impossible. In the western basin, the deposits thin out towards the present day depocenter in the east (Fig. 2(a)). East of a delta area influenced by gas blanking, where older MTDs underly EH-C (Fig. 2(b)), the landslide deposit fills-in an undulating palaeobathymetry, levelling the lake floor towards its present-day, nearly flat morphology. Near the coring site WOER18-L5, individual MTDs are imaged by transparent-to-chaotic seismic facies (Fig. 2(a) and (b)). These bodies pinch out into a high-amplitude reflection package. No clear landslide scar can be identified from the seismic data in the western basin. In contrast, slide scars of well-defined individual MTDs exist in the middle and eastern basin. There, individual landslides occur both on sedimentary sequences covering the lateral slopes of the basin (Fig. 2(d)), as well as along an intra-basinal ridge separating the Reifnitz basin from the Klagenfurt basin (Fig. 2(c)). Other than the deposits of EH-B, which originate exclusively on steep ($> 15^\circ$) slopes, event C also exhibits failure on slopes as gentle as 3° , for instance at the eastern end of the western basin near Pörschach. Overall, the EH-C MTDs amount to a volume of at least $\sim 28.7 \times 10^6 \text{ m}^3$, covering an area of $\sim 6.6 \times 10^6 \text{ m}^2$ and exhibiting an average thickness of $\sim 4.3 \text{ m}$. In all basins, the MTDs are overlain by a megaturbidite, with low-amplitude internal reflectivity and ponding geometries. This megaturbidite is up to 2.6 m thick (Fig. 4; overall volume $\sim 1.9 \times 10^6 \text{ m}^3$) and flattens the rough MTD surface to some extent. The total deposits attributed to EH-C (MTDs and megaturbidites) amount to $\sim 30.6 \times 10^6 \text{ m}^3$.

Sediment core data

Lithostratigraphy

The general lithostratigraphic succession of Wörthersee recovered at coring location WOER18-L5 (see Fig. 1 for coring location) can be subdivided into three main lithostratigraphic units from top to bottom (Fig. 5). Lithostratigraphic unit I (LU-I; 0 – 0.5 m core depth) consists of annually-laminated (varved) sediments. Based on varve thickness, presence of authigenic calcite, organic content and colour, this unit can be further subdivided into two subunits: Unit 1a (LU-Ia; varve thickness $> 1 \text{ mm}$; abundant authigenic calcite, little organic content) and unit 1b (LU-Ib; varve thickness $< 1 \text{ mm}$; hardly any authigenic calcite, increased organic content).

Lithostratigraphic unit IIa (LU-IIa) is composed of dark, non-laminated, organical-rich (gyttja-like) sediments (0.5 – 1.75 m). Unit IIb (LU-IIb) consists of well-laminated, calcite-rich deposits (like LU-Ia), and interbedded parts of non-laminated dark organic mud (1.75 – 5.1 m) The transition between the two subunits is gradual. Several degassing cracks and low-

density values ($\sim 1-1.2 \text{ g/cm}^3$) further reflect the organic content of these units. Magnetic susceptibility is generally low ($5-10 \text{ SI} \times 10^{-5}$) with a few spikes up to $35 \text{ SI} \times 10^{-5}$.

Lithological unit III (LU-III) consists of entirely different, light grey sediments laminated at a mm-scale. At the boundary of LU-IIb to LU-III (5.1 m core depth), both density and magnetic susceptibility increase rapidly. Density rises from ~ 1.25 to 1.5 g/cm^3 and reaches values as high as 2 g/cm^3 further down-core. Magnetic susceptibility increases to values of about $25 \text{ SI} \times 10^{-5}$.

The sedimentary changes indicated by optical and physical properties are further corroborated by grain-size measurements and smear slide analysis (Fig. 6): LU-IIa and LU-IIb range from coarse to very coarse silt and have a clay content below 1%, whereas LU-III consists of fine-to-medium silt and has a clay content of 5 to 10%. Under the microscope, LU-II has a rather heterogenic appearance, mainly consisting of diatoms, amorphous organic matter and calcite crystals. LU-III, on the other hand, consists almost exclusively of silt- to clay-sized particles and has a low amount of organic matter.

Identifying and dating of landslide events in cores

Within the uppermost lithological unit, LU-Ia, two graded beds of about 3 cm thickness, separated by a bright lamina, are recovered (Fig. 7). They contain large organic macro remains and are interpreted as turbidites resulting from near-shore landslides. The short-lived radionuclide data from core WOER18-L5-SC proves the annual character of the calcite-rich laminae: $\sim 22 \pm 1$ laminae can be counted by the unaided eye between the ^{137}Cs -peaks of AD1986 and AD1963. The two turbidites of this core thus are dated to about AD1987 but occurred a year apart.

A more prominent turbidite of ~ 30 cm thickness occurs in cores WOER17-14, WOER17-02 and WOER18-L5-SC, at approximately 50 cm core depth, and therefore can be traced all over the western lake basin. Its lithofacies varies from a coarse, sandy base (~ 5 cm in core WOER17-02), showing multiple pulses, to a fine-grained, homogeneous grey sediment with abundant organic matter at the top. Radiocarbon dating of terrestrial plant material in laminated background sediment of LU-Ib revealed an age range of AD1331 – AD1441 (2σ range) just 3 cm above this turbidite.

The base of the most prominent, 3.7 m thick MTD recovered from the long core WOER18-L5 between 5.3 and 9 m core depth and within the uppermost part of LU-III, consists of rounded to sub-angular gravels ranging from 0.5 cm to about 3 cm in size, which are interspersed in a silty matrix (Fig. 5). Physical properties exhibit a sharp density-contrast to the underlying silts. The biggest gravel clasts are present at the top of the ~ 16 cm thick basal interval of the MTD, that is overlain by a ~ 23 cm thick, sandy turbidite showing three fining-upward cycles. The central part of the MTD is composed of a 1 m thick mudclast conglomerate: soft clasts of 4-5 cm in diameter, composed of LU-III lithology are disseminated in a fine, dense matrix, and are clearly visible in X-CT data and false-colour optical images (Fig 5(b)). The top of the deposit is represented by a 2.3 m thick megaturbidite deposit, which is not entirely homogeneous but shows fluctuations in both density and magnetic susceptibility.

A radiocarbon date about 18 cm above the megaturbidite indicates an age of 13480 – 13733BP, revealing a Late Glacial age for LU-III.

Core-to-Core and Core-to-Seismic Correlation

Lithostratigraphical correlation of the prominent marker layers and the different lithological units enables robust core-to-core correlation across the basin (Fig. 5). Comparison of the seismic reflection pattern to the γ -density and CT-scans (radiodensity) allows for the precise correlation of long core WOER18-L5 (and short core WOER18-L5-SC) to the seismic stratigraphy (Fig. 5). The MTD associated with EH-C clearly correlates to the 3.7 m thick deposit ranging from 5.3 to 9 m core depth, with the basal gravel layer exhibiting a strong seismic reflector.

The 30 cm thick turbidite in the core correlates to the seismically-resolved megaturbidite associated with EH-B, whereas the core-to-seismic and core-to-core correlation for the uppermost part of the sequence (that is subject to strong compaction in the cores) reveals that EH-A does not link to one single simultaneous landslide event, but is actually the result of several, non-concurrent landslides, which all took place after ~AD1950.

Detailed landslide morphology: integrating multibeam bathymetry and seismic data

62 individual landslides (including landslides that are part of the Velden MTC) are observable in the multibeam bathymetric map in total. Most of these can be attributed to either EH-A or EH-B, as inferred from core-to-seismic correlation and basin-wide event horizon mapping (Figs. 8, 9, 10). The deposits of EH-C are covered by about 5 or more meters of sediment that smoothed the hummocky MTD surface morphology. Therefore, there is hardly any morphological expression left of the MTDs related to EH-C in today's bathymetry; only their slide scars are still partly visible in the multibeam bathymetric map (Fig. 8). Moreover, as the MTDs of EH-C extend over the entire basin plains, it is often unclear how many individual slope segments failed. In the following subchapters, some landslides exhibiting peculiar morphological features will be discussed and characterized in detail. The most important morphometrical parameters are listed in table 2.

Eastern basin

In the eastern basin, 3 landslides differing strongly in their morphology occur in close vicinity to each other (Fig. 8): the Krumpendorf east landslide (KEL), exhibiting strong disintegration and a multitude of blocks; the Krumpendorf west landslide (KWL), with a horseshoe morphology showing frontal breaching; and the Sekirn landslide (SL), showing a horseshoe morphology with intact compressional ridges.

The main deposit of the Krumpendorf east landslide (KEL; Fig. 8(a)) is characterized by a concentric morphology, outlined by compressional ridges, and an extensive zone of rafted blocks surrounded by landslide matrix (Fig. 8(a,b)). These blocks spread over an area of 49200 m², extending about 140 m out of the main depositional zone. Only a small impact depression (0.5 m max. depth) is present adjacent to an upslope bedrock ridge, which protrudes about 10 m from the basin plain. Several of these bedrock ridges cross the evacuation zone, leading to steps (max. 45°) in the slide scar, which otherwise shows a slope gradient of 10 – 13° and gently levels out into the basin plain. The main MTD is underlain by

an older (EH-C) MTD that shows frontal thrusting, but does not ramp up from its initial basal shear surface (frontally confined landslide; Moernaut & De Batist 2011), leading to a topographic bulge in the subsurface. The basal shear surface (BSS) of the KEL follows the stratigraphic level defined by the top of this frontally confined landslide in the subsurface of the main deposit and ramps up in the stratigraphy by about 1 m where scattered blocks are present.

The BSS of the Krumpendorf west landslide (KWL; Fig. 8(c,d)) follows the top of an MTD (EH-C) as well, before ramping up about two metres in the stratigraphy, but in contrast to the KEL, this BSS gently dips basinward. The KWL shows a large impact depression (max. depth 0.6 m) and high (up to 2.5 m) lateral compressional ridges (Fig. 8(c,d)). Some scattered blocks are present in front of a 56 m wide frontal breaching zone, spreading over an area of about 9500 m². The evacuated length is considerably longer than that of the KEL (236 m vs. 108 m) and the maximum deposit thickness is almost double that of the KEL (4.9 m vs. 2.7 m). Some of the landslide mass spilled laterally to the east (marked with black arrows in Fig. 8(c)). There, the sediments moved along the gentle slope, progressively disintegrating to form a frontally emergent MTD.

The Sekirn landslide (SL; Fig. 8(c,e)) differs considerably from the KEL and KWL, because it exhibits an intact, 2.3 m high frontal compressional ridge and a small impact depression (0.5 m compared to the present-day lake floor), giving it a perfect horse-shoe morphology. Flow-path analysis as well as considerations on slide scar roughness and limited lateral extent of the SL indicate that the upslope area (light grey in Fig. 8(c)) cannot constitute the evacuated zone of the SL, because (1) there is a significant misfit between the large excavation volume and the small impact zone, (2) bedrock ridges cause a positive morphology in a N-S direction, diverting a potential sediment flow to the north-east (grey arrow in Fig. 8(c)) and (3) the area has a smooth surface, indicating a significant sediment drape, which is not visible in the scars of the coeval KEL and KWL. Instead, in the 30 m high cliff bordering the impact zone, a small niche is present. This niche might either have been created during a rockfall from the cliff or host enough space for sediment to accommodate and fail. However, considering the narrow bedrock ridges in the eastern basin, which do not show a substantial sedimentary drape, the latter explanation seems unlikely.

Western basin

The Velden MTC (Fig. 9(a)), which has already been introduced in the section on seismic landslide stratigraphy, defines the structure of the lake bottom in the very west, spreading over an area of $\sim 0.7 \times 10^6$ m². Several amalgamated MTDs attribute to the complex morphology consisting of multiple frontal and lateral compressional ridges, rafted blocks, as well as smooth surfaces in local depocenters, where megaturbidites pond depressions in underlying rough MTC surfaces. Some slope segments of up to 380 m in length failed almost entirely, leaving only small areas of unfailed upper slope sediments behind, whereas other slopes, including deltaic bodies, remained intact. The sidewalls and headscarps of most landslides are about 4 m high.

The Töschling West landslide (TWL) shows a highly complex evacuation area, with multiple downstepping, staircase-type scars along a terraced slope (Fig. 9(b)). The slope gradient changes drastically from the nearshore area (19°), to the terrace (1°) and along the lower slope (32° to 7°). The depositional area is characterized by a large, semi-circular compression ridge covering an area of $46 \times 10^3 \text{ m}^2$ without an apparent frontal breaching zone. Large (up to 80 m wide) blocks, probably originating from lower slope failures, are dispersed on the landslide lobe. The deposits are pinching out at two different stratigraphical intervals (Fig. 9(c)), indicating two superimposed MTDs ('MTD-stack'), the older (TWL-I) of which correlates stratigraphically to EH-B. Part of the younger MTD (TWL-II) levels out the impact depression of the older landslide.

The big lobe (lobe 1 in Fig. 9(d)) of the Töschling East landslide (TEL) on the other hand, has a well-developed, 1.5 m high compressional ridge and an internal depression zone. Together with the smaller lobe, which has a blocky appearance, the deposit constitutes a single MTD, covering an area of $30 \times 10^3 \text{ m}^2$. The presence of two depositional lobes is due to a bedrock ridge present in the lower slope, splitting the flow path. The scar width of the Töschling East landslide increases from ~ 70 m at the upper slope to about 160 m at the lower slope (Fig. 9(d)).

Anthropogenic landslides

The Bad Saag landslide (BSL; Fig. 10(a,b,c,d)) of 2013, already introduced above, led to the failure of several 1000 m^3 of onshore sediment along a 106 m broad scar with 4.5 m high sidewalls. Impact on the basin plain led to a 2 m deep depressional zone. The sediments spread over an area of $44 \times 10^3 \text{ m}^2$ and led to a turbiditic current, which can be recovered as a 1 cm thick turbidite about 650 m away from the main depositional area (Fig. 10(c); see Fig. 1 for location of core WOER17-14).

The Seefels landslide (SEL) originates in a very narrow (10 m) onshore area and shows a downslope-diverging slide scar, reaching a maximum width of 45 m (Fig. 10(e)). Most of the dispersed landslide mass was either deposited on the lower slope or at the toe of a small gully, covering an area of $\sim 3.5 \times 10^3 \text{ m}^2$. Some of the remobilized sediment might have triggered minor failures at the very base of the slope (zone indicated by yellow dashed lines in Fig. 10(e)).

The deposits of the Pörschach landslide (PL; Fig. 10(f)) are dispersed over an area of $28 \times 10^3 \text{ m}^2$ along a terraced slope. They show heavy disintegration and follow a slide scar of an older MTD, related to EH-B. Only a small number of blocks made it into the deep basin. The slide scar can be traced onshore, originating in a narrow area (~ 15 m wide) and spreading downslope along a morphology defined by bedrock ridges.

The Dellach landslide (DL; Fig. 10(g)) only eroded the uppermost meter of sediment, contrasting the deep (4-5 m) landslide scars of most landslides in Wörthersee, including the Bad Saag, Seefels and Pörschach landslides. In the nearshore area, the narrow scar (20 m) is blurred by a rough lake-floor-morphology showing several small-scale irregularities. Downslope, the slide scar branches out into individual sub-scars.

Discussion

Preconditioning and trigger of landslides in Wörthersee

Several preconditioning factors can increase the landslide-susceptibility of slopes, for instance (1) excess pore pressure and underconsolidation due to rapid deposition of sediments (Prior *et al.* 1982); (2) weak layers (Locat *et al.* 2014 and references therein) or (3) oversteepened slopes (Piper & McCall 2003). The ultimate slope failure is caused by the combination of these prerequisites with short-term triggering mechanisms such as (1) loading of slopes, either associated with human activity (Assier-Rzadkiewicz *et al.* 2000), subaerial rockfalls (Kremer *et al.* 2015; Daxer *et al.* 2018) or heavy rainfall (Longva *et al.* 2003); (2) lake level fluctuations (Anselmetti *et al.* 2009) and, most importantly, (3) earthquakes (Schnellmann *et al.* 2002; Simonneau *et al.* 2013; Van Daele *et al.* 2015; Normandeau *et al.* 2016).

Based on our estimates and the drastic lithological change from LU-III to LU-II (i.e. from light-grey, well-laminated fine-grained sediments to coarser deposits with high amount of authigenic calcite and organic matter), as well as the characteristic change from ponding to draping geometries across the boundary of SU-2 to SU-1 (described in many other formerly glaciated peri-alpine lakes, e.g. Daxer *et al.* 2018 and references therein), we interpret the transition from LU-III to LU-II (and the correlating changeover from SU-2 to SU-1; Fig. 5) as the Late-Pleistocene to Holocene transition, when the lake switched from a glacial meltwater influenced lake to a peri-alpine lake dominated by hemipelagic sedimentation. The sedimentation rates during the deposition of SU-2 (thickness > 43 ms) exceeded 4-5 mm/year, assuming glacier-free lake basins at 20.000 BP and a seismic velocity of 1500 m/s. In the Holocene, the sedimentation rates decrease considerably to about 0.5 mm/year. This lithological succession closely resembles that of many other previously glaciated depositional basins exhibiting large-scale landsliding, be it fjords (Aarseth *et al.* 1989; Hjelstuen *et al.* 2009; Hjelstuen & Brendryen 2014) or lakes (Chapron *et al.* 1996; Reusch *et al.* 2016; Strupler *et al.* 2017). It has been shown that high sedimentation rates (> 1 mm/yr) and low permeability can inhibit a normal consolidation process during sedimentation, leading to the generation of shallow pore fluid overpressure (Dugan & Germaine 2008; Dugan & Sheahan 2012). Underconsolidation and a reduced shear strength due to overpressure (e.g. Stigall & Dugan 2010; Wiemer *et al.* 2015) in the Late Glacial LU-III may be one of the reasons why EH-B and EH-C differ so strongly in remobilised volume (1:5.5), source area of failure (steep slopes vs. slope & intra-basin) and consequently flow evolution (megaturbidite vs. mass flow/megaturbidite). Because the sidewall height of most landslides visible in the multibeam bathymetry is in the range of 1.5 – 4.5 m and sedimentation rates are generally lower on slopes (Blais & Kalff 1995), failure of these MTDs most likely occurred in Late Glacial clays or at the transition to LU-II. This is similar to findings in Lake Lucerne (Strasser *et al.* 2007) and Lake Zurich (Strupler *et al.* 2017), indicating further dependence of slope initiation on lithological variability and the possible presence of predefined weak layers in the LU-III stratigraphy.

Coevality (within the limits of seismic resolution) of landslides with different source areas, as seen in EH-B and EH-C, has proven to be a good indicator of a seismic trigger mechanism (Schnellmann *et al.* 2002; Praet *et al.* 2017; Moernaut *et al.* 2019). As indicated by a radiocarbon age (AD1331 – AD1441), the AD1348 earthquake constitutes a likely trigger of the multiple landslides related to EH-B. This earthquake is the largest seismic event historically recorded in the entire Alps (Stucchi *et al.* 2013) and led to massive rockslides at the nearby Dobratsch mountain (Lenhardt 2007). The reported intensities (EMS-98) of this earthquake were around VIII-IX at the lake site (Hammerl 1994; Stucchi *et al.* 2013). Compared with studies on lacustrine paleoseismology, this is well above the empirical intensity threshold (seismic intensities \geq VI) for seismically triggered landslides (Monecke *et al.* 2004; Van Daele *et al.* 2015). Therefore, a causal relationship between the AD1348 earthquake and EH-B is very likely. Similar assumptions can be made for EH-C dated to approximately 13700 cal BP, which is represented by synchronous landslides on an even larger scale. The fact that all lake basins (and subbasins) failed at about the same time can only be explained by either a very local major seismic event or a sudden drop in lake level. The lithological change from fine-grained, bright grey mm-scale laminae (LU-III) to darker coloured, more organically rich sediments (LU-II) a few centimetres above the turbidite deposit related to EH-C indicates a major change in lake system dynamics and sedimentation after the landslide event. A concomitant drop in lake level, however, is unlikely due to the lack of visible erosional surfaces in the seismic data at shallow water depths, thus favouring an earthquake trigger.

Human induced landslides

Since the youngest mass movements cannot be attributed to the AD1976 Friuli earthquake ($M_w \sim 6.5$) constituting the most recent major ($M_w > 6$) earthquake in the region, an anthropogenic trigger is a likely explanation for the Bad Saag, Seefels, Pörschach and Dellach landslides. Indeed, for the BSL, loading of slopes during building activity is documented as the cause of failure initiation. In the 1980s, piers were built in the headscarp area of the SFL and the DL, probably leading to the small-scale slope failures visible in the bathymetry and accounting for the rough lake floor at the DL. These landslides are also a very likely source for the turbidites visible in core WOER18-L5-SC (Fig. 7). For the bigger Pörschach landslide, the construction of a boathouse seems to be the triggering event. The slide scar developed from a small, point source failure and propagates downslope along a bedrock ridge, leading to a larger-scale subaqueous failure. Similar observations have been made for the Oberrieden slide in Lake Zurich (Strupler *et al.* 2018). This MTD, as well as the well-studied anthropogenic Horgen slide, however, are much bigger in volume (Oberrieden: $1.49 \times 10^6 \text{ m}^3$, Horgen: $1.29 \times 10^6 \text{ m}^3$; Sammartini *et al.*, in press) than the human-induced landslides in Wörthersee. The development of large translational landslides from point sources in Wörthersee is largely hindered by bedrock ridges, which act as lateral boundaries to failure propagation. Just as for the Bad Saag landslide, the evacuation zone of the SEL, PL and DL extends onshore, making this the distinctive feature compared to the older non-anthropogenic (EH-B) events, where the headscarp is well below the water level ($> 15 \text{ m}$ water depth).

Factors controlling landslide morphology

The morphology of landslides in Wörthersee seems to be mainly controlled by three driving forces: (1) slope gradient of the evacuation zone and changes therein; (2) preconditioning of the impacted area by previous landslides; and (3) the remobilised sediment volume.

The most significant difference between the two “end-members” of landslide morphologies observed in the eastern basin, the heavily disintegrated KEL and the horseshoe-shaped SL, is the slope gradient (14° vs. 73°). Steeper slope gradients generally cause higher impact velocities (depending on height drop), and therefore lead to stronger deformation of basin-plain sediments and frontal thrusts. In contrast to the deposits originating from very steep ($>45^\circ$) slopes in Aysén fjord (Lastras *et al.* 2013; Van Daele *et al.* 2013), however, the SL does not show a distal unconfined part. This might be explained by (1) the drastic change in slope gradient at the toe of slope, not allowing the kinetic energy of the (possibly very small) impactor to be transferred into lateral movement of basin-plain sediment (Mazzanti & De Blasio 2010), (2) different types of impactors, i.e. onshore debris entrained in a mass-flow in Aysén vs. bedrock material from an underwater cliff in Wörthersee, and (3) the much larger height drop at the Aysén fjord (> 195 m, excluding the onshore part; Van Daele *et al.* 2013). The landslide morphology of the Bad Saag landslide supports the second explanation: similar to the Aysén mass-flow, coarse, already disintegrated material mixed with hemipelagic sediment impacted on the basin plain during the BSL, resulting in a deep depressional zone, but still managed to emerge distally for a considerable distance. The KWL, showing high compressional ridges as well as a few rafted blocks, represents an intermediate member of landslide morphology. Here, the change of slope gradient is not as extreme as for the SL, but greater than for the KEL (17° vs. 10°).

Aside from the slope gradient, the variations in flow development and disintegration could also be linked to the morphology of the impacted zone: upon impact, both the KEL as well as the KWL remobilized basin-plain sediment along a shear surface developed at the lithological boundary between older MTDs time-correlative to EH-C and the overlying sedimentary sequence. Whereas at the location of KWL this shear surface is gently inclined along the path of travel and thus facilitated the remobilized mass to plough into the basin-plain sediment, the same surface on top of a frontally-confined Late Glacial MTD exhibits a slightly positive upward bend at KEL, likely facilitating ramping up and disintegration.

Another type of preconditioning of the depositional area is seen at the Töschling West slides, where the first event, which probably resembled the single MTD of Töschling East, got overprinted by subsequent events. The impact depression of TWL-I was filled by TWL-II and the compressional ridge was partly buried by the lower slope failure.

Run-out length has generally been found to be proportional to failure volume (e.g. Gee *et al.* 1999; Moernaut & De Batist 2011). This explains the long run-out of the Velden MTC and of the landslides related to EH-C. For the latter, the high content of clay-sized minerals probably contributed to the high-mobility (Longva *et al.* 2003), facilitating propagation even on an almost flat basin plain. For such massive landslides to happen along slopes or onshore, enough sediment potentially ready to fail needs to be present. In the Velden area, this is guaranteed by several inflows, leading to active recharge of slopes.

Conclusions

In the present study, we depicted the dimensions, morphology and unravelled the date of several landslides in glacialic Würthersee by means of reflection seismic mapping of MTDs, coring of MTDs and their respective turbidites, and analysis of multibeam bathymetric data. Based on these studies, we come to the following general (1, 2) and site-specific (3-5) conclusions:

- (1) Preconditioning of the landslide impact area by previous mass movements can have a strong influence on landslide morphology: the top of an older MTD can act as the basal shear surface, altering the propagation path of a landslide;
- (2) Deformation and erosion of basin-plain sediments is depending on (1) slope gradient of the slide scar and changes therein; (2) excavation height; (3) the type of impactor (hemipelagic sediment, (onshore) mass flows, hard rock);
- (3) Human-induced landslides in Würthersee were all initiated onshore, but downslope failure propagation partly resulted in a larger subaqueous landslide;
- (4) Rapid sedimentation of fine-grained glaciolacustrine sediments in the Late Glacial allowed for extensive landsliding ($\sim 28.7 \times 10^6 \text{ m}^3$) in Würthersee. This is relevant for all types of glacialic basins that show a similar lithological evolution;
- (5) The AD1348 earthquake probably triggered numerous landslides, including a large ($\sim 4.5 \times 10^6 \text{ m}^3$) mass transport complex in the western basin.

Acknowledgements

This project was funded by the Austrian Science Fund (FWF), project number P30285-N34, and the Austrian Academy of Sciences project “S⁴SLIDE-Austria”. Maddalena Sammartini acknowledges funding from the European Union’s Horizon 2020 research and innovation program under the Marie-Sklodowska-Curie grant agreement No 721403. We acknowledge ETH Zurich for access to the Kullenberg coring system and platform and we are very grateful to all the people who helped carrying out fieldwork and retrieving Kullenberg-cores on Würthersee: Michael Hilbe, Reto Seifert and Patrick Oswald. The Research Department for Limnology (ILIM, Mondsee) and Hannes Höllner are thanked for providing the research vessel Luna and logistical help, as is the Carinthian Institute of Lake Research (KIS). The multibeam data was kindly provided by the state of Carinthia (Land Kärnten, Abteilung Umwelt, Energie und Naturschutz). Further acknowledged are Irka Hajdas for radiocarbon analyses and Pascal Rünzi for both radionuclide dating and helping during field work. We are very grateful to Markus Erhardt, Gerald Degenhart and Wolfgang Recheis for the use of the medical CT scanner at the Medical University of Innsbruck. IHS Markit is thanked for its educational grant program providing the KINGDOM seismic interpretation software. We thank Marc De Batist, an anonymous reviewer and Jason Chaytor for their constructive comments on an earlier version of this manuscript.

References

- Aarseth, I., Lønne, Ø. & Giskeødegard, O. 1989. Submarine slides in glaciomarine sediments in some western Norwegian fjords. *Marine Geology*, **88**, 1–21, [https://doi.org/10.1016/0025-3227\(89\)90002-9](https://doi.org/10.1016/0025-3227(89)90002-9).
- Anderle, N. 1977. Geologische Karte der Republik Österreich 1:50000, 201-210 Villach-Assling. 1.
- Anselmetti, F.S., Ariztegui, D., et al. 2009. Environmental history of southern Patagonia unravelled by the seismic stratigraphy of Laguna Potrok Aike. *Sedimentology*, **56**, 873–892, <https://doi.org/10.1111/j.1365-3091.2008.01002.x>.
- APA/derStandard. 2013. Kärnten: Erdrutsch bei ÖBB-Baustelle riss Straße weg. <https://www.derstandard.at/story/1385170631020/erdrutsch-bei-oebb-baustelle-strasse-am-woerthersee-nordufer-weggerissen>.
- Assier-Rzadkiewicz, S., Heinrich, P., Sabatier, P.C., Savoye, B. & Bourillet, J.F. 2000. Numerical Modelling of a Landslide-generated Tsunami: The 1979 Nice Event. *Pure and Applied Geophysics*, **157**, 1707–1727, <https://doi.org/10.1007/PL00001057>.
- Blais, J.M. & Kalff, J. 1995. The influence of lake morphometry on sediment focusing. *Limnology and Oceanography*, **40**, 582–588, <https://doi.org/10.4319/lo.1995.40.3.0582>.
- Bondevik, S., Løvholt, F., Harbitz, C., Mangerud, J., Dawson, A. & Svendsen, J.I. 2005. The Storegga Slide tsunami - Comparing field observations with numerical simulations. *Marine and Petroleum Geology*, **22**, 195–208, <https://doi.org/10.1016/j.marpetgeo.2004.10.003>.
- Chapron, E., Van Rensbergen, P., Beck, C., De Batist, M. & Paillet, A. 1996. Lacustrine sedimentary records of brutal events in Lake Le Bourget (Northwestern Alps-Southern Jura). *Quaternaire*, **7**, 155–168, <https://doi.org/10.3406/quate.1996.2068>.
- Clare, M., Chaytor, J., et al. 2018. A consistent global approach for the morphometric characterization of subaqueous landslides. *Geological Society, London, Special Publications*, **8**, SP477.15, <https://doi.org/10.1144/SP477.15>.
- Conrad, O., Bechtel, B., et al. 2015. System for Automated Geoscientific Analyses (SAGA) v. 2.1.4. *Geoscientific Model Development*, **8**, 1991–2007, <https://doi.org/10.5194/gmd-8-1991-2015>.
- Daxer, C., Moernaut, J., Taylor, T., Haas, J.N. & Strasser, M. 2018. Late Glacial and Holocene sedimentary infill of Lake Mondsee (Eastern Alps, Austria) and historical rockfall activity revealed by reflection seismics and sediment core analysis. *Austrian Journal of Earth Sciences*, <https://doi.org/10.17738/ajes.2018.0008>.
- Dugan, B. & Germaine, J.T. 2008. Near-seafloor overpressure in the deepwater Mississippi Canyon, northern Gulf of Mexico. *Geophysical Research Letters*, <https://doi.org/10.1029/2007GL032275>.
- Dugan, B. & Sheahan, T.C. 2012. Offshore sediment overpressures of passive margins: Mechanisms, measurement, and models. *Reviews of Geophysics*, **50**, <https://doi.org/10.1029/2011rg000379>.
- Enet, F., Grilli, S.T. & Watts, P. 2003. Laboratory Experiments for Tsunamis Generated by Underwater Landslides: Comparison with Numerical Modeling. *In: Proceedings of the*

Thirteenth (2003) International Offshore and Polar Engineering Conference (ISOPE03, Honolulu, USA, May 2003). 372–379.

- Gee, M.J.R., Masson, D.G., Watts, A.B. & Allen, P.A. 1999. The Saharan debris flow: An insight into the mechanics of long runout submarine debris flows. *Sedimentology*, **46**, 317–335, <https://doi.org/10.1046/j.1365-3091.1999.00215.x>.
- Girardclos, S., Schmidt, O.T., Sturm, M., Ariztegui, D., Pugin, A. & Anselmetti, F.S. 2007. The 1996 AD delta collapse and large turbidite in Lake Brienz. *Marine Geology*, <https://doi.org/10.1016/j.margeo.2007.03.011>.
- Hammerl, C. 1994. The earthquake of January 25th, 1348, discussion of sources. *Historical Investigation of European Earthquakes. Materials of the CEC project "Review of Historical Seismicity in Europe"*, **2**, 225–240.
- Hjelstuen, B.O. & Brendryen, J. 2014. Submarine mass movements and trigger mechanisms in Byfjorden, western Norway. In: *Advances in Natural and Technological Hazards Research*. Springer Netherlands, 351–359., https://doi.org/10.1007/978-3-319-00972-8_31.
- Hjelstuen, B.O., Haflidason, H., Sejrup, H.P. & Lyså, A. 2009. Sedimentary processes and depositional environments in glaciated fjord systems - Evidence from Nordfjord, Norway. *Marine Geology*, **258**, 88–99, <https://doi.org/10.1016/j.margeo.2008.11.010>.
- Homann, O. 1962. Die geologisch-petrographischen Verhältnisse im Raume Ossiachersee - Wörthersee (südlich Feldkirchen zwischen Klagenfurt und Villach). *Jahrbuch der Geologischen Bundesanstalt*, **105**, 243–272.
- Hühnerbach, V. & Masson, D.G. 2004. Landslides in the North Atlantic and its adjacent seas: An analysis of their morphology, setting and behaviour. *Marine Geology*, **213**, 343–362, <https://doi.org/10.1016/j.margeo.2004.10.013>.
- Kahler, F. 1962. Geologische Karte der Umgebung von Klagenfurt 1:50000. 1.
- Kelts, K., Briegel, U., Ghilardi, K. & Hsu, K. 1986. The limnogeology-ETH coring system. *Swiss Journal of Hydrology*, **48**, 104–115, <https://doi.org/10.1007/BF02544119>.
- KIS. 2019. Wörthersee. http://www.kis.ktn.gv.at/188551_DE-Kaerntner_Seen-Seenseite.?seeid=46.
- Krastel, S., Behrmann, J.-H., et al. (eds). 2014. *Submarine Mass Movements and Their Consequences*. Cham, Springer International Publishing, Advances in Natural and Technological Hazards Research, <https://doi.org/10.1007/978-3-319-00972-8>.
- Kremer, K., Corella, J.P., Adatte, T., Garnier, E., Zenhäusern, G. & Girardclos, S. 2015. Origin of turbidites in deep Lake Geneva (France-Switzerland) in the last 1500 years. *Journal of Sedimentary Research*, **85**, 1455–1465, <https://doi.org/10.2110/jsr.2015.92>.
- L'Heureux, J.-S., Longva, O., et al. 2012. Identification of Weak Layers and Their Role for the Stability of Slopes at Finneidfjord, Northern Norway. In: *Submarine Mass Movements and Their Consequences*. Dordrecht, Springer Netherlands, 321–330., https://doi.org/10.1007/978-94-007-2162-3_29.
- Lastras, G., Amblas, D., et al. 2013. Landslides cause tsunami waves: Insights from aysén

- fjord, Chile. *Eos*, **94**, 297–298, <https://doi.org/10.1002/2013EO340002>.
- Lenhardt, W.A. 2007. Earthquake-Triggered Landslides in Austria-Dobratsch Revisited. *Jahrbuch der Geologischen Bundesanstalt*, **147**, 193–199.
- Locat, J., Leroueil, S., Locat, A. & Lee, H. 2014. Weak Layers: Their Definition and Classification from a Geotechnical Perspective. *In: Submarine Mass Movements and Their Consequences, 6th International Symposium*. Kluwer Academic Publishers, 3–12., https://doi.org/10.1007/978-3-319-00972-8_1.
- Longva, O., Janbu, N., Blikra, L.H. & Bøe, R. 2003. The 1996 Finneidfjord Slide; Seafloor Failure and Slide Dynamics. 531–538., https://doi.org/10.1007/978-94-010-0093-2_58.
- Masson, D.G., Harbitz, C.B., Wynn, R.B., Pedersen, G. & Løvholt, F. 2006. Submarine landslides: Processes, triggers and hazard prediction. *Philosophical Transactions of the Royal Society A: Mathematical, Physical and Engineering Sciences*, **364**, 2009–2039, <https://doi.org/10.1098/rsta.2006.1810>.
- Mazzanti, P. & De Blasio, F. V. 2010. Peculiar morphologies of subaqueous landslide deposits and their relationship to flow dynamics. *Submarine Mass Movements and Their Consequences - 4th International Symposium*, 141–151, <https://doi.org/10.1007/978-90-481-3071-9>.
- Moernaut, J. & De Batist, M. 2011. Frontal emplacement and mobility of sublacustrine landslides: Results from morphometric and seismostratigraphic analysis. *Marine Geology*, **285**, 29–45, <https://doi.org/10.1016/j.margeo.2011.05.001>.
- Moernaut, J., Van Daele, M., et al. 2019. The subaqueous landslide cycle in south-central Chilean lakes: The role of tephra, slope gradient and repeated seismic shaking. *Sedimentary Geology*, **381**, 84–105, <https://doi.org/10.1016/j.sedgeo.2019.01.002>.
- Monecke, K., Anselmetti, F.S., Becker, A., Sturm, M. & Giardini, D. 2004. The record of historic earthquakes in lake sediments of Central Switzerland. *Tectonophysics*, **394**, 21–40, <https://doi.org/10.1016/j.tecto.2004.07.053>.
- Normandeau, A., Lamoureux, S.F., Lajeunesse, P. & Francus, P. 2016. Sediment dynamics in paired High Arctic lakes revealed from high-resolution swath bathymetry and acoustic stratigraphy surveys. *Journal of Geophysical Research: Earth Surface*, **121**, 1676–1696, <https://doi.org/10.1002/2016JF003873>.
- Owen, M., Day, S. & Maslin, M. 2007. Late Pleistocene submarine mass movements: occurrence and causes. *Quaternary Science Reviews*, **26**, 958–978, <https://doi.org/10.1016/j.quascirev.2006.12.011>.
- Piper, D.J.W. & McCall, C. 2003. A Synthesis of the Distribution of Submarine Mass Movements on the Eastern Canadian Margin. *In: Locat, J., Mienert, J. & Boisvert, L. (eds) Submarine Mass Movements and Their Consequences: 1st International Symposium*. Dordrecht, Springer Netherlands, 291–298., https://doi.org/10.1007/978-94-010-0093-2_32.
- Piper, D.J.W., Cochonat, P. & Morrison, M.L. 1999. The sequence of events around the epicentre of the 1929 Grand Banks earthquake: initiation of debris flows and turbidity current inferred from sidescan sonar. *Sedimentology*, **46**, 79–97,

<https://doi.org/10.1046/j.1365-3091.1999.00204.x>.

- Pistotnik, J., Daurer, A., et al. 1980. Die östlichen Zentralalpen (südlich der Hohen Tauern und östlich der Katschberg-Linie). In: *Der Geologische Aufbau Österreichs*. Springer Vienna, 348–404., https://doi.org/10.1007/978-3-7091-3744-4_19.
- Pope, E.L., Talling, P.J., Carter, L., Clare, M.A. & Hunt, J.E. 2017. Damaging sediment density flows triggered by tropical cyclones. *Earth and Planetary Science Letters*, **458**, 161–169, <https://doi.org/10.1016/j.epsl.2016.10.046>.
- Praet, N., Moernaut, J., et al. 2017. Paleoseismic potential of sublacustrine landslide records in a high-seismicity setting (south-central Alaska). *Marine Geology*, **384**, 103–119, <https://doi.org/10.1016/j.margeo.2016.05.004>.
- Prior, D.B., Coleman, J.M. & Bornhold, B.D. 1982. Results of a known seafloor instability event. *Geo-Marine Letters*, **2**, 117–122, <https://doi.org/10.1007/BF02462751>.
- Reusch, A., Moernaut, J., Anselmetti, F.S. & Strasser, M. 2016. Sediment mobilization deposits from episodic subsurface fluid flow-A new tool to reveal long-term earthquake records? *Geology*, **44**, 243–246, <https://doi.org/10.1130/G37410.1>.
- Rzadkiewicz, S.A., Mariotti, C. & Heinrich, P. 1996. Modelling of submarine landslides and generated water waves. *Physics and Chemistry of the Earth*, **21**, 7–12, [https://doi.org/10.1016/S0079-1946\(97\)00002-5](https://doi.org/10.1016/S0079-1946(97)00002-5).
- Sammartini, M., Moernaut, J., Anselmetti, F.S., Hilbe, M., Lindhorst, K., Praet, N. & Strasser, M. n.d. An Atlas of Mass-Transport Deposits in Lakes. In: Ogata, K., Festa, A. & Pini, G. A. (eds) *Submarine Landslides: Subaqueous Mass Transport Deposits from Outcrops to Seismic Profiles*. American Geophysical Union, 384.
- Schindelin, J., Arganda-Carreras, I., et al. 2012. Fiji: an open-source platform for biological-image analysis. *Nature Methods*, **9**, 676–682, <https://doi.org/10.1038/nmeth.2019>.
- Schmidt, R., Weckström, K., Lauterbach, S., Tessadri, R. & Huber, K. 2012. North Atlantic climate impact on early late-glacial climate oscillations in the south-eastern Alps inferred from a multi-proxy lake sediment record. *Journal of Quaternary Science*, **27**, 40–50, <https://doi.org/10.1002/jqs.1505>.
- Schnellmann, M., Anselmetti, F.S., Giardini, D., McKenzie, J.A. & Ward, S.N. 2002. Prehistoric earthquake history revealed by lacustrine slump deposits. *Geology*, **30**, 1131, [https://doi.org/10.1130/0091-7613\(2002\)030<1131:PEHRBL>2.0.CO;2](https://doi.org/10.1130/0091-7613(2002)030<1131:PEHRBL>2.0.CO;2).
- Schnurrenberger, D., Russell, J. & Kelts, K. 2003. Classification of lacustrine sediments based on sedimentary components. *Journal of Paleolimnology*, **29**, 141–154, <https://doi.org/10.1023/A:1023270324800>.
- Schultze, E. 1984. Neue Erkenntnisse zur spät- und frühpostglazialen Vegetations- und Klimaentwicklung im Klagenfurter Becken. *Carinthia II*, **174**, 261–266.
- Schulz, L., Schönhuber, M., Santner, M. & Swaton, T. 2008. Erhebung des Ist-Zustandes der Uferverbauung und Seeinbauten des Wörthersees und des Millstätter Sees. *Publikationen des Kärntner Instituts für Seenforschung*, **4**, 1–13.
- Seguinot, J., Ivy-Ochs, S., Jouvét, G., Huss, M., Funk, M. & Preusser, F. 2018. Modelling

- last glacial cycle ice dynamics in the Alps. *The Cryosphere*, **12**, 3265–3285, <https://doi.org/10.5194/tc-12-3265-2018>.
- Simonneau, A., Chapron, E., et al. 2013. Mass-movement and flood-induced deposits in Lake Ledro, southern Alps, Italy: Implications for Holocene palaeohydrology and natural hazards. *Climate of the Past*, **9**, 825–840, <https://doi.org/10.5194/cp-9-825-2013>.
- Stigall, J. & Dugan, B. 2010. Overpressure and earthquake initiated slope failure in the Ursa region, northern Gulf of Mexico. *Journal of Geophysical Research*, **115**, 1–11, <https://doi.org/10.1029/2009jb006848>.
- Strasser, M., Stegmann, S., Bussmann, F., Anselmetti, F.S., Rick, B. & Kopf, A. 2007. Quantifying subaqueous slope stability during seismic shaking: Lake Lucerne as model for ocean margins. *Marine Geology*, **240**, 77–97, <https://doi.org/10.1016/j.margeo.2007.02.016>.
- Strasser, M., Monecke, K., Schnellmann, M. & Anselmetti, F.S. 2013. Lake sediments as natural seismographs: A compiled record of Late Quaternary earthquakes in Central Switzerland and its implication for Alpine deformation Weissurt, H. (ed.). *Sedimentology*, **60**, 319–341, <https://doi.org/10.1111/sed.12003>.
- Strupler, M., Hilbe, M., Anselmetti, F.S., Kopf, A.J., Fleischmann, T. & Strasser, M. 2017. Probabilistic stability evaluation and seismic triggering scenarios of submerged slopes in Lake Zurich (Switzerland). *Geo-Marine Letters*, **37**, 241–258, <https://doi.org/10.1007/s00367-017-0492-8>.
- Strupler, M., Anselmetti, F.S., Hilbe, M. & Strasser, M. 2018. Quantitative characterization of subaqueous landslides in Lake Zurich (Switzerland) based on a high-resolution bathymetric dataset. *Geological Society, London, Special Publications*, SP477.7, <https://doi.org/10.1144/SP477.7>.
- Stucchi, M., Rovida, A., et al. 2013. The SHARE European Earthquake Catalogue (SHEEC) 1000–1899. *Journal of Seismology*, **17**, 523–544, <https://doi.org/10.1007/s10950-012-9335-2>.
- Sue, L.P., Nokes, R.I., Davidson, M.J., Nokes, R.I. & Davidson, M.J. 2011. Tsunami generation by submarine landslides: comparison of physical and numerical models. **11**, 133–165, <https://doi.org/10.1007/s10652-010-9205-9>.
- Talling, P.J., Clare, M., Urlaub, M., Pope, E., Hunt, J.E. & Watt, S.F.L. 2014. Large submarine landslides on continental slopes: Geohazards, methane release, and climate change. *Oceanography*, **27**, 32–45, <https://doi.org/10.5670/oceanog.2014.38>.
- Tappin, D.R., Watts, P. & Grilli, S.T. 2008. The Papua New Guinea tsunami of 17 July 1998: anatomy of a catastrophic event. *Hazards Earth Syst. Sci*, **8**, 243–266.
- Twichell, D.C., Chaytor, J.D., ten Brink, U.S. & Buczkowski, B. 2009. Morphology of late Quaternary submarine landslides along the U.S. Atlantic continental margin. *Marine Geology*, **264**, 4–15, <https://doi.org/10.1016/j.margeo.2009.01.009>.
- Urgeles, R. & Camerlenghi, A. 2013. Submarine landslides of the Mediterranean Sea: Trigger mechanisms, dynamics, and frequency-magnitude distribution. *Journal of Geophysical Research: Earth Surface*, **118**, 2600–2618,

<https://doi.org/10.1002/2013JF002720>.

- Urgeles, R., Bahk, J.-J., et al. 2019. Tsunami hazard from submarine landslides: scenario-based assessment in the Ulleung Basin, East Sea (Japan Sea). *Geosciences Journal*, **23**, 439–460, <https://doi.org/10.1007/s12303-018-0044-x>.
- Van Daele, M., Versteeg, W., Pino, M., Urrutia, R. & De Batist, M. 2013. Widespread deformation of basin-plain sediments in Aysén fjord (Chile) due to impact by earthquake-triggered, onshore-generated mass movements. *Marine Geology*, **337**, 67–79, <https://doi.org/10.1016/j.margeo.2013.01.006>.
- Van Daele, M., Moernaut, J., et al. 2015. A comparison of the sedimentary records of the 1960 and 2010 great Chilean earthquakes in 17 lakes: Implications for quantitative lacustrine palaeoseismology. *Sedimentology*, <https://doi.org/10.1111/sed.12193>.
- Wiemer, G., Moernaut, J., et al. 2015. The role of sediment composition and behavior under dynamic loading conditions on slope failure initiation: a study of a subaqueous landslide in earthquake-prone South-Central Chile. *International Journal of Earth Sciences*, **104**, 1439–1457, <https://doi.org/10.1007/s00531-015-1144-8>.
- Yokoyama, R., Shirasawa, M. & Pike, R.J. 2002. Visualizing topography by openness: A new application of image processing to DEMs. *Photogrammetric Engineering & Remote Sensing*, **68**, 257–265.

Figure captions

Fig. 1. (a) Bathymetric map of Wörthersee, located at the south-eastern rim of the European Alps, Austria (see inset). The lake is divided into three main basins: the western basin (WB), the middle basin (MB; including the Kapuziner basin, KAB) and the eastern basin, consisting of the Reifnitz sub-basin (RB) and the Klagenfurt sub-basin (KB). Red lines indicate the main faults (dashed where inferred; according to Austrian Geological maps: Kahler 1962; Anderle 1977). (b) Seismic survey grid showing profiles acquired using a 3.5 kHz source (red lines) and a ~8 kHz source (black lines).

Fig. 2. 3.5 kHz reflection seismic profiles along the main lake axis (a, b, c) and perpendicular to it (d). See Fig. 1(a) for location of seismic lines. (a) Seismic profile along the western basin. 3 main event horizons are distinguished (EH-A, EH-B and EH-C). EH-A is in the stratigraphically highest position, only overlain by a thin (max. 0.5 ms) reflection package. EH-B and EH-C show extensive landsliding, especially in the west, with the MTDs of EH-C covering almost the whole lake basin and being overlain by a ~3 m thick megaturbidite (light orange). (b) Close-up of Fig. 2(a) at the long coring site WOER18-L5. The MTD associated with EH-C is underlain by older MTDs and exhibits lateral variation in seismic facies, indicating smaller, local MTDs. (c) Seismic profile along the eastern basin. As in the western basin, EH-C covers most of the lake basin, but individual landslides can be more easily distinguished due to step-ups of the basal shear surface (BSS) and distinct changes in seismic facies where landslides intersect. At the ridge separating the Reifnitz basin from the Klagenfurt basin, a draped failure scar of EH-C is clearly visible. (d) Profile perpendicular to the eastern basin's main axis. A prominent failure scar can be traced along a terrace overridden by a landslide of EH-C.

Fig. 3. (a) 3.5 kHz reflection seismic profile perpendicular to the lake axis in the western basin. The reflections of seismic unit 1 form a drape which also covers slopes as steep as 20°. Seismic unit 2 shows reflections onlapping onto the acoustic basement, indicating a ponding sedimentation. Colour coding as in Fig. 2. (b) Correlation of 8 kHz reflection seismic profiles in the deepest part of the

western and eastern basins, respectively. Note the different vertical axes, indicating higher sedimentation rates in the western basin.

Fig. 4. Thickness maps of landslide events related to EH-B and EH-C. For both event horizons, mapping of the landslide base was restricted in the very west due to indistinct changes in seismic facies and limited penetration of the seismic signal. Blue arrows indicate inferred flow direction of individual landslides attributed to event horizon EH-C. To ensure comparability, the same scale (0-16 m) was chosen, although the maximum thickness of the MTDs associated with EH-B is only ~12 m.

Fig. 5. (a) Seismic to core correlation, geophysical data and lithology of long core WOER18-L5 and core to core correlation of short cores WOER17-14, WOER17-02 and WOER18-L5-SC. Small turbidites (< 10 cm) correlating to EH-A are present in cores WOER17-14 and WOER18-L5-SC, but too small to be visible in the core log. The blue interval corresponds to MTDs or megaturbidites of EH-B, the red interval to those of EH-C. White stars denote radiocarbon samples, white triangles grain-size samples and brown triangles indicate smear slide samples. (b) CT data showing the base of the MTD related to EH-C and the distribution of gravel in the sediment (extracted from the CT data). Note the similar radiodensity of mudclasts to background sediment below the base. The optical image has been modified (histogram equalization) to enhance contrast.

Fig. 6. (a) Grain-size measurements on core WOER18-L5 (see Fig. 5(a) for sampling locations). (b) Representative smear slide image of LU-IIa consisting of amorphous organic matter (aom) and diatoms (d). (c) Representative smear slide image of silt-to clay-rich sediments (LU-III).

Fig. 7. Optical image and radionuclide data of short core WOER18-L5-SC. No radionuclide samples were collected in the turbidites (3 – 11.5 cm core depth). Note the bright layer separating the two turbidites at about 7 cm core depth, indicating that the two related landslides occurred a year apart.

Fig. 8. Landslide morphologies in the eastern basin (see Fig. 1 for locations). (a) Morphology of Krumpendorf East landslide (KEL). The bright linear features on the slopes indicate bedrock ridges crossing the evacuation zone. ID = Impact Depression. (b) Longitudinal seismic profile through KEL, showing a frontally confined landslide (part of EH-C) below. (c) Morphology of landslides Krumpendorf West (KWL) in the north and Sekirn (SL) in the south. Black arrows indicate the flow path of landslide mass that travelled along the gentle slope and did not impact on the basin plain. (d) Longitudinal seismic profile through landslide Krumpendorf West. (e) Longitudinal seismic profile through landslide Sekirn.

Fig. 9. Landslide morphologies in the western basin (see Fig. 1 for location). (a) Morphology of the Velden MTC. (b) Morphology of landslide Töschling West. Note the staircase-type slide scars. (c) Seismic profile perpendicular to landslide Töschling West. An older MTD (related to EH-B) is overlain by a younger MTD, pinching out higher in the seismic stratigraphy. (d) Morphology of landslide Töschling East. BRR = bedrock ridge. (e) Seismic profile perpendicular to landslide Töschling East.

Fig. 10. Landslide morphologies of human-induced landslides (see Fig. 1 for location). (a) Morphology of Bad Saag landslide (BSL). (b) Photograph of the onshore headscarp of BSL (courtesy of Christoph Posch, ÖBB). (c) Photograph of core WOER17-14 directly after acquisition (see Fig. 1 for location). The annual layers on top of the turbidite related to the Bad Saag landslide are clearly visible. (d) Longitudinal seismic profile through the Bad Saag landslide. (e) Morphology of Seefels landslide (SEL). White arrow indicates main flow path, yellow arrow the assumed flow path of the outlier blocks (b). BRR = bedrock ridge, b = blocks. (f) Morphology of Pörschach landslide (PL).

Note the older slide scars and deposits related to EH-B. (g) Morphology of landslide Dellach. Next to the recent landslide, the slide scar of an older event can easily be recognized.

ACCEPTED MANUSCRIPT

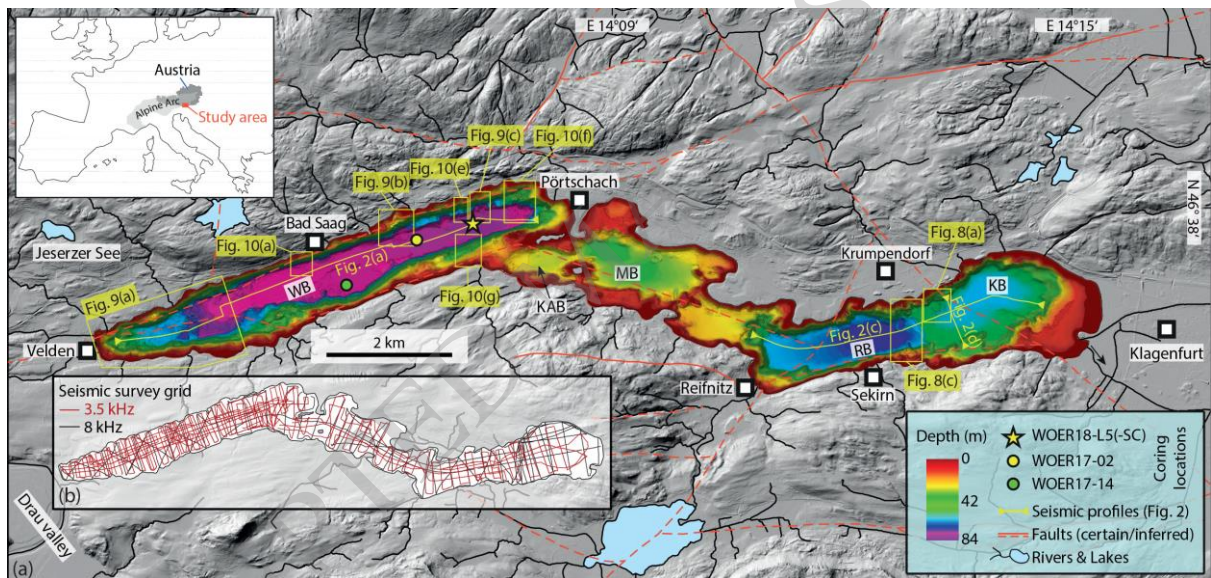
Table 1. *Radiocarbon ages from organic macro-remains*

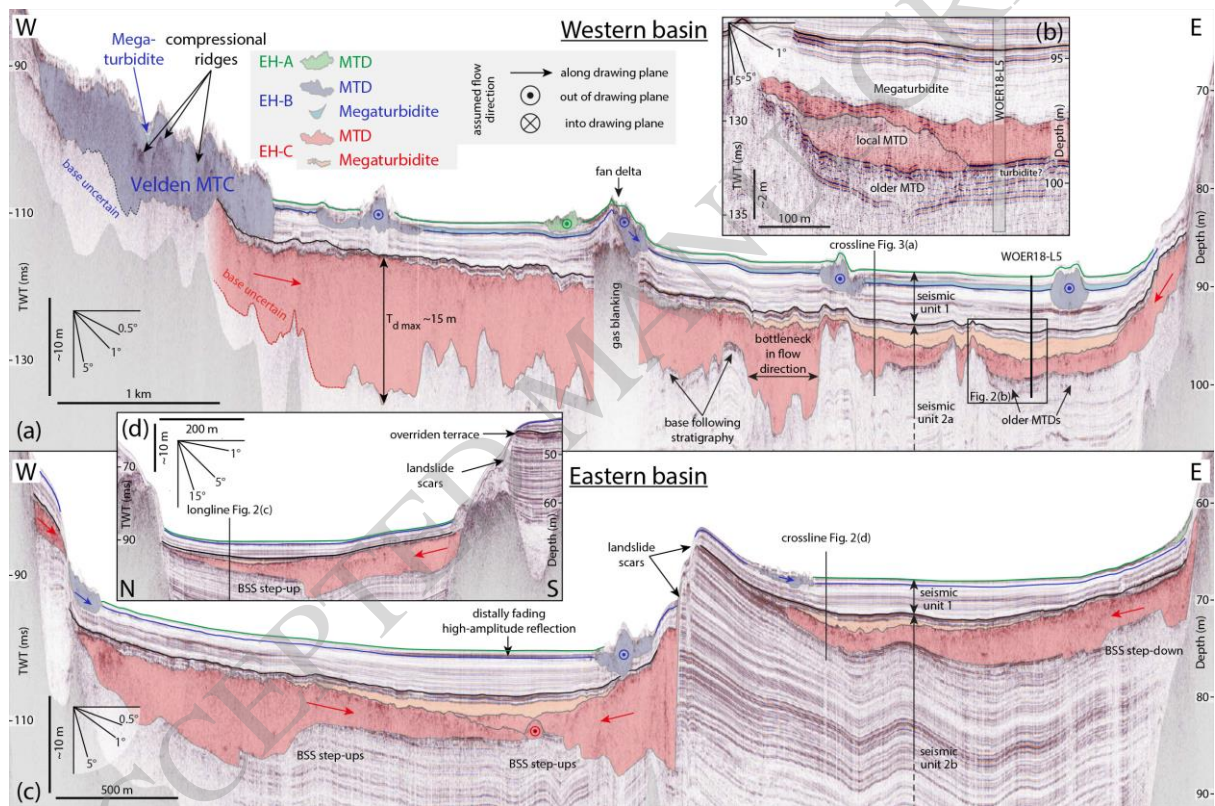
Sediment core	Sediment core depth (cm)	Section	Sediment core section depth (cm)	Lab No.	Conventional radiocarbon age (¹⁴ C yr BP)	2σ calibration (cal. yr BP)	2σ calibration (BC/AD)	Dated material
WOER17-02	32.5 – 35.5	-	32.5 – 35.5	ETH-88627	388 ± 30		1442 - 1632	Betula fruits, plant macro remains
WOER17-02	46 – 51	-	46 – 51	ETH-85092	519 ± 23		1331 - 1441	Betula fruits, plant macro remains
WOER17-02	129 – 131	-	129 – 131	ETH-85093	2562 ± 24		-804 - 588	leaf
WOER18-L5	222	F	8.5 – 9.5	ETH-96546	6938 ± 25	7832 – 7693		plant macro remains
WOER18-L5	344	F	127 – 128	ETH-96545	5273 ± 24	6179 – 5944		plant macro remains
WOER18-L5	452	E	96 – 97	ETH-96547	9952 ± 28	11600 – 11251		plant macro remains
WOER18-L5	524	D	10 – 11	ETH-96548	11785 ± 27	13733 – 13480		plant macro remains

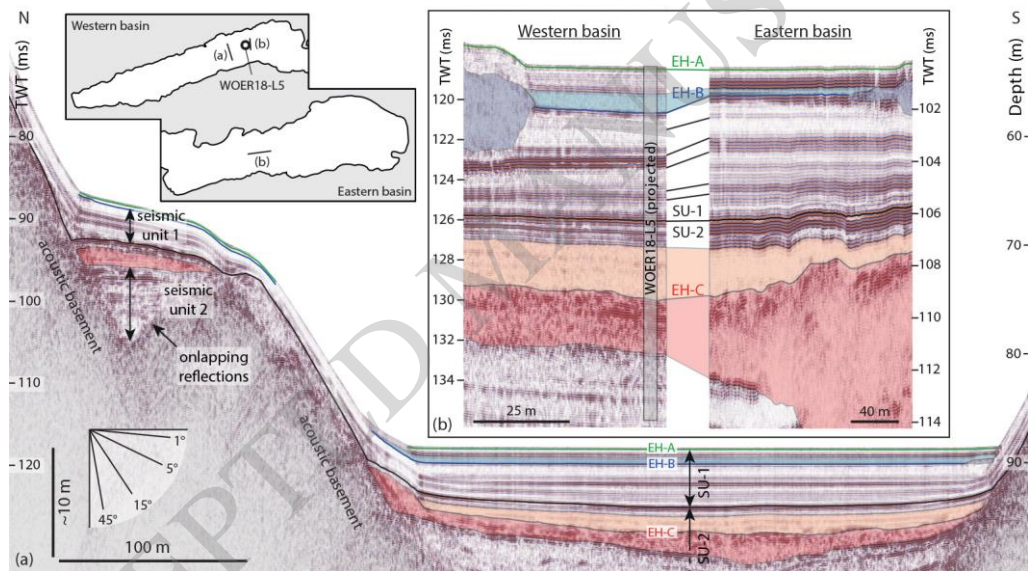
Table 2. *Morphometric data of selected landslides*

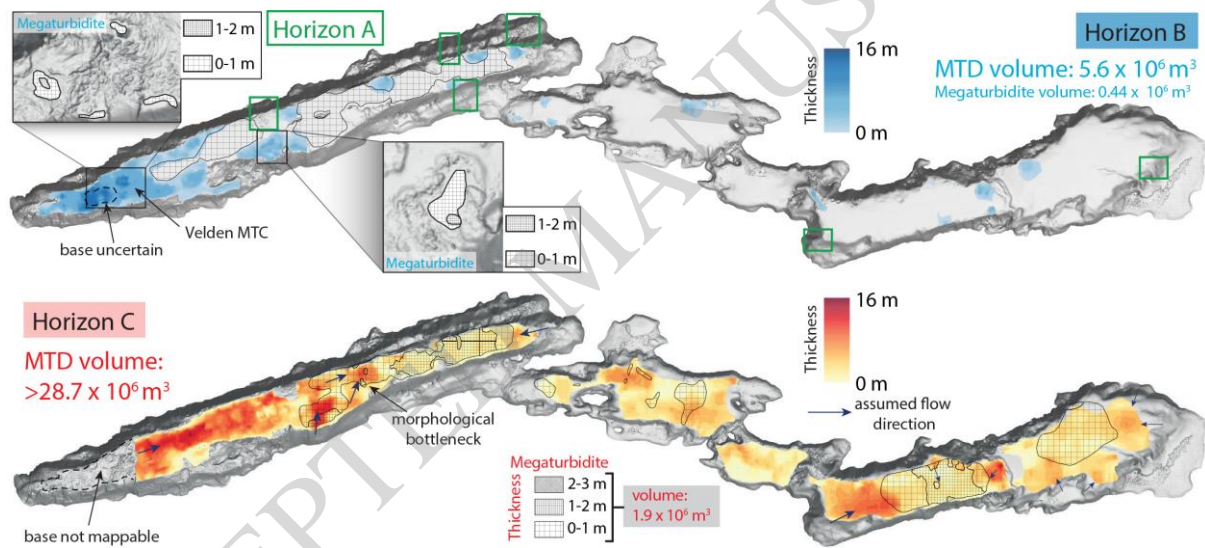
	KEL	KWL	SL	TEL	BSL
Depth below lakefloor (m)	0.675	0.9	0.9	1.35	0.3
Total length Lt (m)	266	425	121	403	385
Deposit length Ld (m)	158	189	112	139.6	227
Evacuated Length (m)	108	236	9	263.4	158
Maximum Length rafted blocks (m)	143	67	0	0	0
Scar perimeter length (m)	475	721	-	673	348
Sidewall height* (m)	~1.6	1.5 – 2 m	-	3.1	3.5
Evacuation height (m)	38	50.5	max. 30	59.5	81
Scar width (m)	194	137	-	167	106
Maximum deposit width (m)	178	245	104	291	200.5
Maximum deposit thickness (m)	2.7	4.9	4.7	4.4	4.5
Total height drop (m)	43.1	54.2	31	60	82.6
Slope gradient (unfailed)	10°	16°	73°	19.2°	18.1°
Slope gradient at the toe	0.2°	0.1°	0.1°	0.1°	0°
Slope gradient change at toe of slope	10°	10 - 17°	73°	11°	36°
Area (m²)	71205	56300	11030	32810	43730
Volume (m³)	79034	96309	26896	92600	68885

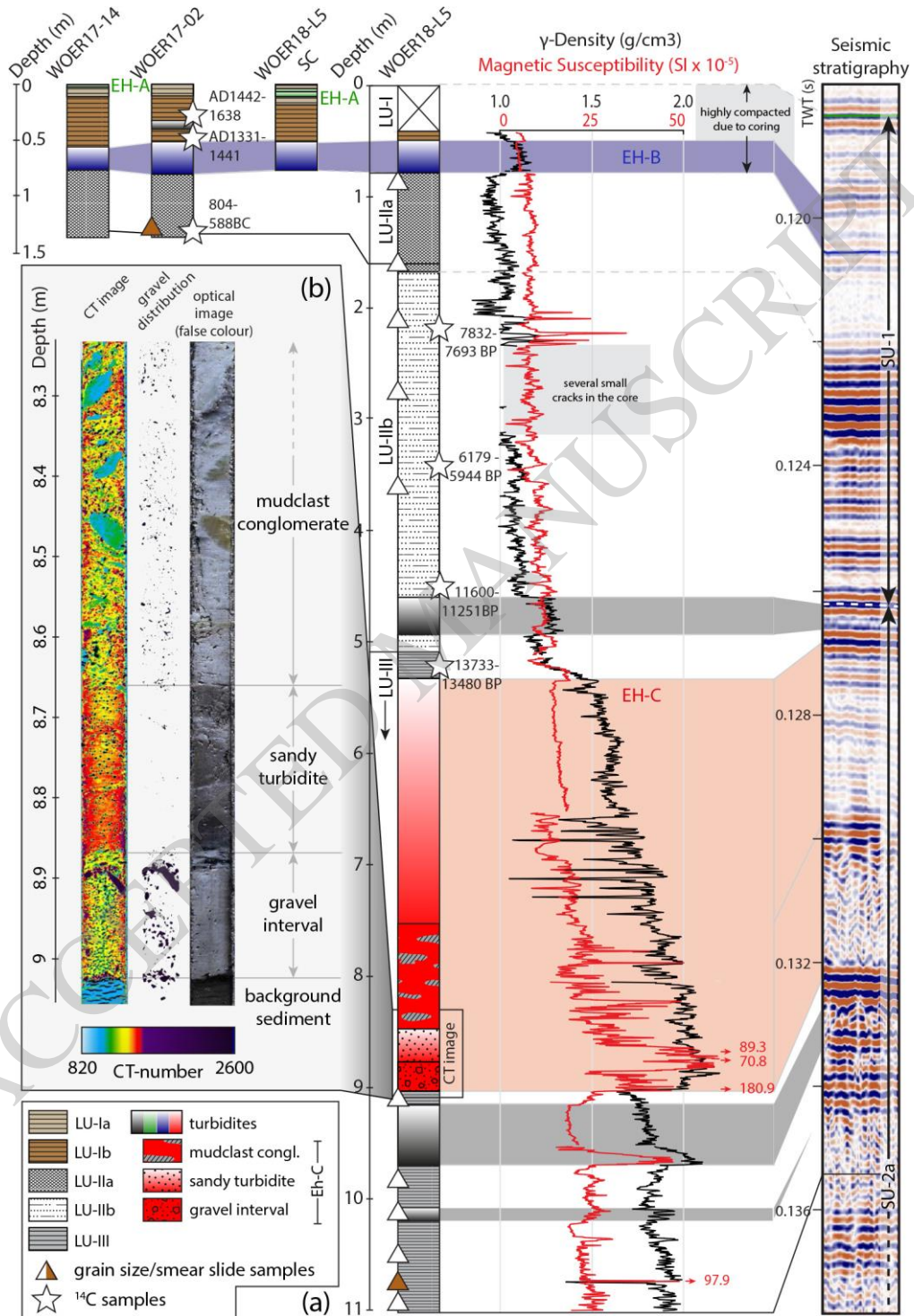
Morphometric data was measured according to Clare et al. (2018). KEL = Krumpendorf East landslide; KWL = Krumpendorf West landslide; SL = Sekirn landslide; TEL = Töschling East landslide; BSL = Bad Saag landslide. Note that the sidewall height (*) was measured instead of the headscarp height, because no well-developed headscarps are visible in the bathymetric data.

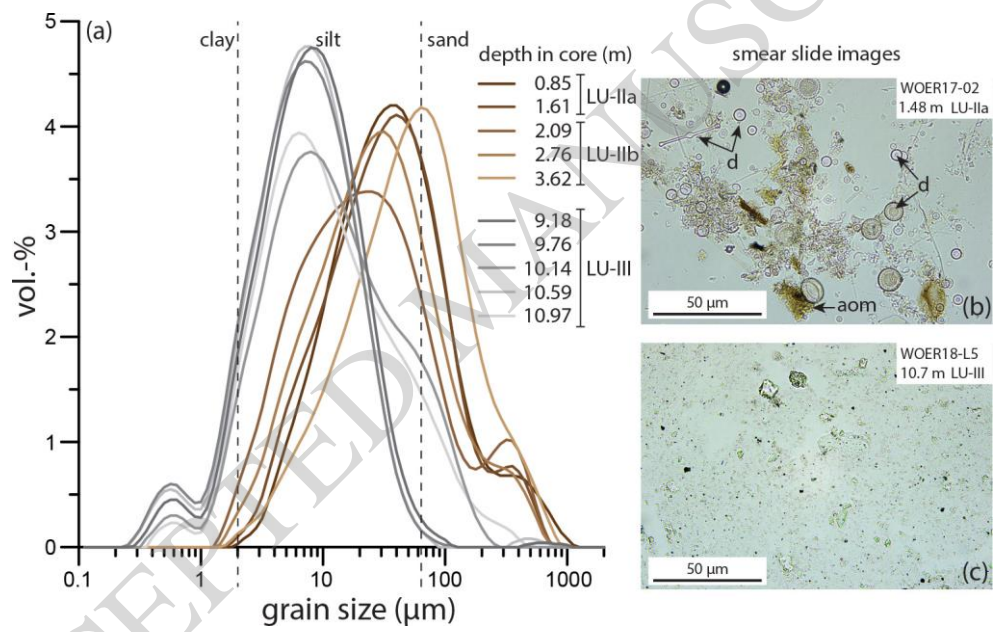


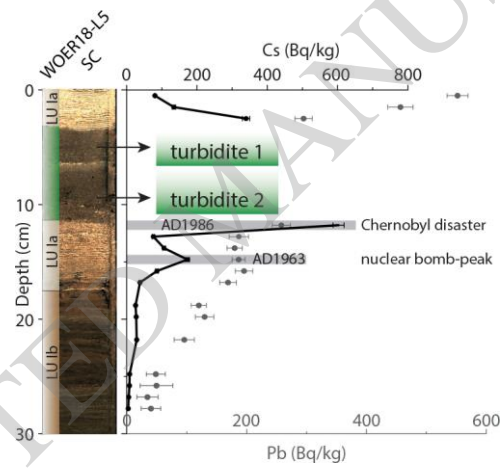


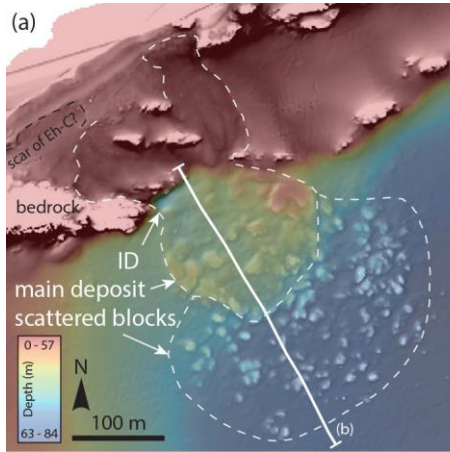




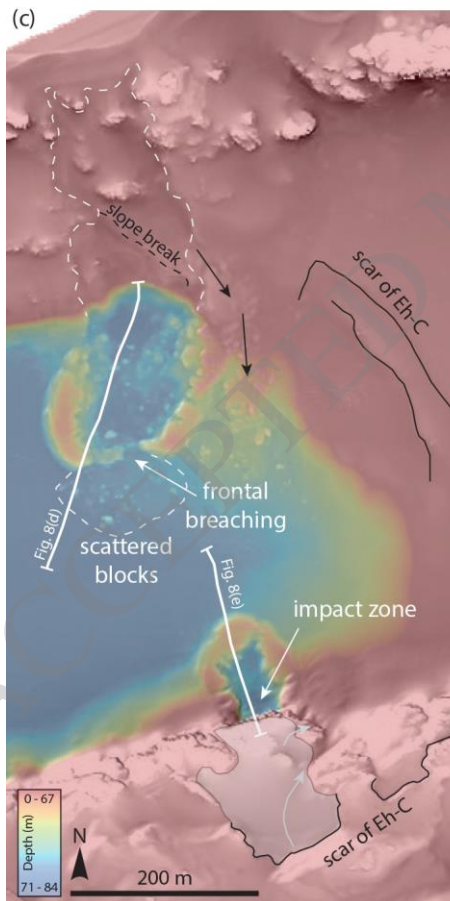
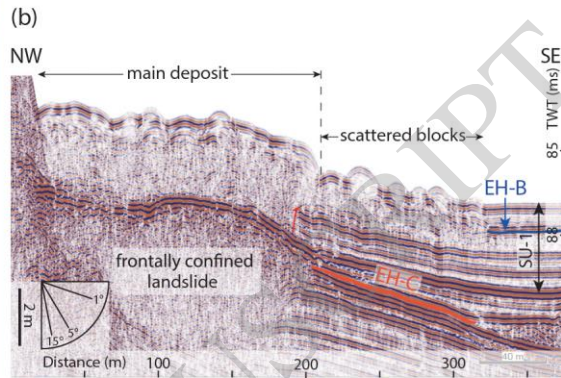




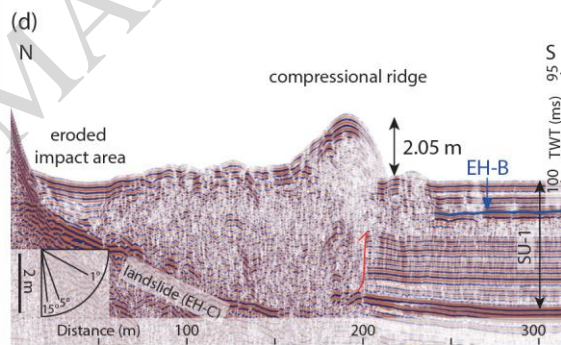




Krumpendorf East - Rafted blocks



Krumpendorf West - Impact MTD & Frontal breaching



Sekirn - Impact MTD with intact ridge

